Double Layer at [BuMeIm][Tf_2N] Ionic Liquid–Pt or –C Material Interfaces

Céline Cannes, Hubert Cachet, Catherine Debiemme-Chouvy, Claude Deslouis, Jacques Sanoit (de), Claire Le Naour, Veronika A. Zinovyeva

To cite this version:

Céline Cannes, Hubert Cachet, Catherine Debiemme-Chouvy, Claude Deslouis, Jacques Sanoit (de), et al.. Double Layer at [BuMeIm][Tf_2N] Ionic Liquid–Pt or –C Material Interfaces. Journal of Physical Chemistry C, 2013, 117, pp.22915-22925. 10.1021/jp407665q . hal-00935837

HAL Id: hal-00935837
https://hal.sorbonne-universite.fr/hal-00935837

Submitted on 3 May 2019

Double Layer at [BuMeIm][Tf₂N] Ionic Liquid–Pt or −C Material Interfaces

Céline Cannes*†, Hubert Cachet‡, Catherine Debiemme-Chouvy‡, Claude Deslouis‡, Jacques de Sanoit§, Claire Le Naour†, and Veronika A. Zinovyeva†

† Institut de Physique Nucléaire, CNRS, Université Paris-Sud 11, 91406 Orsay Cedex, France

‡ CNRS, UPR 15, Laboratoire Interfaces et Systèmes Electrochimiques, Université Pierre et Marie Curie, 75005 Paris, France

§ CEA, LIST, Diamond Sensors Laboratory, 91191 Gif-sur-Yvette, France

J. Phys. Chem. C, **2013**, *117* (44), pp 22915–22925

*Tel.: +33 169157152. Fax: +33 169157150. E-mail: cannes@ipno.in2p3.fr.

Abstract

The interface [BuMeIm][Tf2N]/electrode, where [BuMeIm][Tf2N] stands for the ionic liquid 1-butyl-3-methylimidazolium bis(trifluoromethylsulfonyl)imide, was characterized by electrochemical impedance spectroscopy at different temperatures and for different electrode materials: platinum (Pt, metallic), glassy carbon (GC, high conductivity), carbon nitride (a-CNx, mean conductivity), and boron-doped diamond (BDD, semiconducting with a quasimetallic character). For Pt, GC, and a-CNx, the behavior of the interface could be described by the same equivalent electrical circuit. In the case of BDD, a parallel combination of Rsc and Csc was introduced into the circuit to take into account the potential drop due to the development of a space charge region within the material. The Mott–Schottky plots have confirmed the polycrystalline semiconductor character of the BDD material, and the boron concentration estimated is fully consistent with the B amount introduced for the synthesis. The variations of the double-layer capacitance as a function of potential were found to be camel shaped for all electrode materials at the highest studied temperature. This is consistent with the prediction of Kornyshev's theory as low values of the packing parameter γ were estimated by simulation (lower than 0.33). An increase of the double-layer capacitance is found with the temperature similarly to most of the results obtained for molten salts.

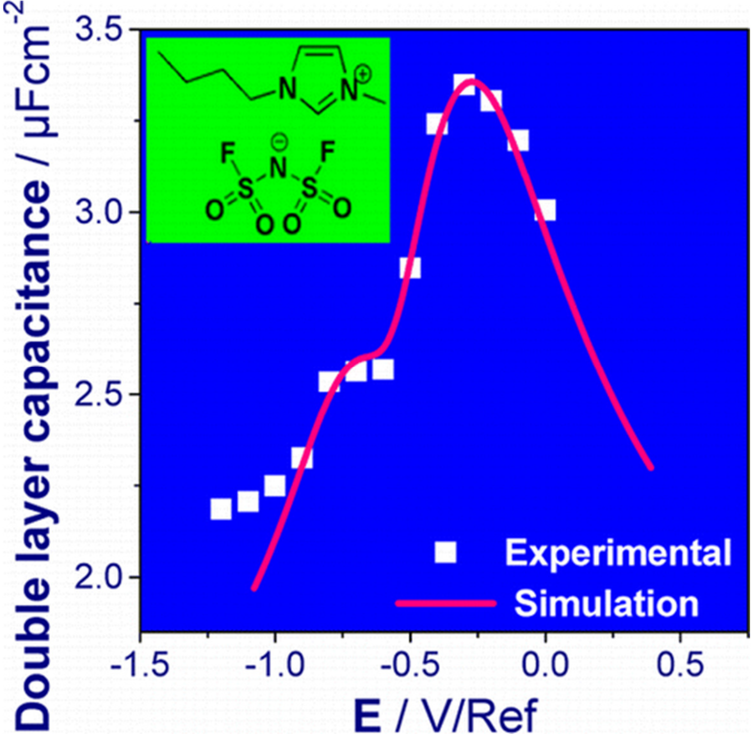

1 Introduction

The structure of the double layer of ionic liquids (ILs) contacting different electrode materials has recently given rise to a huge number of both theoretical (1-18) and experimental works (19-48). The knowledge of its characteristics, which condition in a dramatic way electron transfer is obviously of paramount interest in the development of the manifold applications which are listed in an exhaustive manner in recent reviews (49-54). Among those applications, the knowledge of the properties and characteristics of the double layer of ILs, and concurrently their wide potential window within which the material behaves as a quasi ideally polarizable electrode, is of primary interest in the use of ILs in supercapacitors (55, 56). Facing the abundant literature of experimental works, the theoretical approaches between the three systems, aqueous solutions, molten salts, and ionic liquids, are totally unbalanced: there are in fact no unambiguously accepted theories for both molten salts and ILs at the present time that compare with the well-established Gouy–Chapman–Stern (GCS) theory for aqueous solvents. However, the different and recent above-mentioned theoretical approaches came to a sufficient degree of refinement so that a comparison with experimental works is now wholly justified.

Experimental works in this field are mainly based on double-layer capacitance measurements (25-41) deduced from either electrochemical impedance spectroscopy (EIS) or ac voltammetry and spectroscopic or surface analysis measurements (SFG, surface Raman, or SERS on Ag, SECM, STM/AFM) (42-48) occasionally coupled to electrochemical measurements. If one only considers double-layer capacitance data, there are still debates on the dependence of the capacitance with potential and with temperature on the role of the substrate (metallic or nonmetallic) and on the role of an equivalent of the Helmholtz layer in aqueous solvents which obviously cannot be present with the same characteristics in ILs. This situation is complicated by the fact that for a large number of ILs, purity, in particular concerning the water amount, can be a critical issue.

According to the literature on experimental works, most of the results from EIS or ac voltammetry tend to substantiate the bell shape dependence vs potential of the double-layer capacitance in the case of noble metals. This is namely the case for Au and Pt (25, 48) and also for Au when the potential is moved in the anodic direction for a system showing hysteresis according to the potential variations (41). This shape was also found for Bi(100) (32, 33) for the same cation (1-ethyl-3-methylimidazolium, $EtMeIm^+$) and two different anions. Referring to theoretical works, the proposed explanations are generally based on the concept of the lattice-gas model (1) applicable to these concentrated solutions, for which the specific nature of the cations, formed of a polar part and an organic neutral one, is at the origin of potential voids. The void density may be reduced in the double layer because of the high electric field in this region. Other works show results with camel shape curves (38, 41), namely for Au, the latter reference corresponding to the case when the potential is moved in the cathodic direction. The camel shape has been predicted recently for cations with longer neutral tails, thus liable to increase the number of voids, partly due to the importance of excluded volume effects. In this case, the packing effect due to the electric field in the double layer is more pronounced. In a second panel of works, a parabolic curve with a minimum is observed, but this occurs very often with glassy carbon (GC) electrodes (20, 21, 23, 25, 39, 40). This capacitance vs potential curve was found also for Hg (39), but the minimum of the curve did not correspond to the potential of zero charge (pzc) determined by the same authors from electrocapillary measurements. These two potentials are very often assumed as being the same on solid electrodes. Some works concluded on a quasi independence of the double-layer capacitance with potential (24, 34).

The existence of an inner (compact) layer not yet clearly identified from theoretical predictions is in general highlighted by the spectroscopic measurements mentioned above. It corresponds to a marked change characterized by the exchange of cation and anion adsorption at the electrode/IL interface through the pzc. SFG measurements carried out with the Pt electrode and $EtMeIm^+$cation (47) allowed the author to conclude that the space charge domain close to the interface could be envisioned as a single layer as a Helmholtz layer, capacitance measurements not being conclusive. Restructuring of the surface of single crystals proved by STM (36, 37) around the pzc suggests the role of a strong adsorption and the possible micelle formation induced by matching sizes at the molecular scale.

Finally, the effect of temperature on the double-layer capacitance value was studied in very few works which all concluded to an increase of C_{dl} with temperature (21, 23, 38). This is an opposite result to the prediction of the GCS theory but in agreement with the existing theories for molten salts.

In this work, we carried out an EIS study to analyze the behavior of a well-known IL 1-butyl-3-methylimidazolium bis(trifluoromethanesulfonyl)imide ([BuMeIm][Tf_2N]) in contact with different electrode materials, either metallic (Pt) or carbon based with different charge carrier densities (glassy carbon (GC), carbon nitride (a-CNx), or boron-doped diamond (BDD)). In the latter case, the possible influence of a space charge layer within the material, sometimes claimed for a material such as GC (20), was purposely introduced in well-defined conditions with BDD. Two other carbon materials were also considered, GC and a-CNx, the latter being also envisaged now under nanomaterial form as a possible candidate for supercapacitors (57). By doing so we are able to separate the role of the material and the response of the IL. The a-CNx material was chosen as an electrode material since it was promoted as a possible substitute for BDD in view of its wide potential window, high electrochemical reactivity with respect to outer sphere redox systems, chemical inertness, and ability to be synthesized as pinhole-free thin films (58-63). The influence of temperature (25–56 °C) was also investigated. In particular, we show that the total impedance response in the so-called double-layer domain otherwise called ideally polarizable domain can be analyzed on the basis of a unique equivalent circuit for either metallic (Pt) or different nonmetallic (carbon) electrodes which in the former case contain a huge number of mobile charge carriers or in the latter may behave as a semiconductor (BDD) for which a significant part of the potential drop is located within the material giving rise to a space charge layer.

2 Experimental Conditions

2.1 **Electrodes**

BDD Elaboration

A BDD layer was synthesized at LCD (CEA Saclay) using the microwave plasma-enhanced chemical vapor deposition (MPECVD) method according to the protocol described in refs 64, 66, and 67. The p-Si(100) boron-doped substrate (500 μm thick × 20 cm^2 in area, resistivity < 0.005 Ω cm) was first seeded by spin-coating using an aqueous slurry of PVA and diamond nanoparticles (nominal diameter ~5 nm) in water prior to diamond growth. The diamond growing was then performed using methane diluted in hydrogen (C/H = 0.25%) at a total flow rate of 100 sccm (standard cubic centimeters per minute), a forward power of 1.8 kW, a system pressure of 35 mbar, a substrate temperature of 800 °C, and a growth time of 16 h. Trimethyl boron was used as the boron precursor source with B/C = 8800 ppm. High purity gases were employed, and particularly the ultra pure H precursor was provided by a hydrogen generator, ensuring ultra low nitrogen impurity content (<10 ppb). After the plasma had been turned off, samples were cooled to ambient temperature under hydrogen flow for 2 h. Hydrogen flux was cut after cooling to avoid (or minimize) diamond oxidation. The growth process resulted in a film thickness of 500 nm with a very high boron doping concentration ([B] = 3×10^{21} at cm^{-3}) as calibrated using secondary ion mass spectrometry (SIMS) (see Figure SI1, Supporting Information).

a-CNx Elaboration

a-CNx films have been elaborated by DC magnetron cathodic sputtering from a graphite target in the presence of a reactive argon plasma containing nitrogen. The reactor used was an MP 300 S model from PLASSYS Company. The substrates were 316 L stainless steel sheets (300 μm thick, mass composition %: Fe, 65; Ni, 12.8; Cr, 18.7; Mo, 1.5; Si, 0.5; Mn, 1.5) provided by ARCELOR-MITTAL Company and used as received without further mechanical polishing. They were first sonicated in successive dichloromethane, acetone, and ethanol baths, then chemically etched in H_2O_2 (30%)/H_2SO_4 (95%) mixture (1/2 volume ratio), and finally submitted to an RF (13.56 MHz) ionic etching (substrate + target) in the reactor. The deposition proceeded during 40 min under 1 Pa total gas pressure (nitrogen partial pressure 0.03 Pa) with Ar and N_2 flow rates equal to 12.4

and 0.42 sccm, respectively. The power was set to 200 W. These conditions were characterized earlier to offer the optimal reactivity and potential window in aqueous solution (63).

A glassy carbon plate and platinum sheet were commercially available from Goodfellow.

Electrode Mounting

One square centimeter surface area samples are cut from the different materials (BDD/Si wafer, aCNx/stainless steel sheet, platinum sheet, or glassy carbon plate) and mounted on a copper self-adhesive rubber stuck onto a glass plate (1 cm × 5 cm). The ohmic contact between the back side of the samples and the copper layer was done using eutectic indium–gallium coating. Electrodes were entirely encapsulated into an epoxy resin (Araldite, Bostik S.A., France) leaving only a bare material window (surface <1 cm^2) and a copper electric contact.

Activation of Electrodes

Before use, electrodes were electrochemically activated in different aqueous electrolytes. BDD was activated by a train of short cathodic and anodic current pulses (±10 mA/cm^2/0.1 s) in a cola-based light soda (without caffeine and sugar) as supporting electrolyte (68, 69). The a-CNx and Pt electrodes were activated by cyclic voltammetry (CV) at 0.1 V s^{-1} (10 cycles) between open circuit potential (OCP) and H_2 evolution in 0.5 M H_2SO_4. GC was activated by a train of short cathodic current pulses (−10 mA/cm^2/0.1 s) in 0.5 M H_2SO_4.

2.2 **Chemical Reagents**

The IL [BuMeIm][Tf_2N] is commercially available (Solvionic, purity >99.9%). It was used without further purification and stored in an argon-filled dry glovebox (O_2 concentration < 0.5 ppm and H_2O concentration < 5 ppm). The water concentration measured by coulometric Karl Fischer titration was found equal to 30 ± 5 ppm. Potassium ferricyanide, potassium ferrocyanide trihydrate, potassium chloride (Acros Organics), and silver(I) trifluoromethanesulfonate (Sigma Aldrich) were reagent grade quality and used without additional purification.

2.3 **Electrochemical Measurements**

The electrochemical experiments were carried out with a PGSTAT30 (Metrohm-Ecochemie) potentiostat–galvanostat embodying an impedance module for EIS measurements.

After activation, the improvement of the electrochemical reactivity on the electrodes was checked with CV (decrease of the peak-to-peak potential difference) and with EIS (decrease of the charge transfer resistance (65, 66) at OCP) using $[Fe(CN)_6^{3-/4-}] = 10^{-3}$ M as the redox couple in 0.5 M KCl aqueous electrolyte. After control, the electrodes were thoroughly rinsed with deionized water and ethanol.

Experiments in the IL solutions were performed at 25, 38, 50, and 56 °C ± 1 °C, the temperature being controlled with a thermostat. To attain a stabilized OCP, the three electrodes were immersed into the IL electrolyte more than one hour prior to all measurements. The potential domain analyzed by EIS was first defined by CV. This voltage range was determined by the electrochemical window where the anodic and cathodic currents do not exceed ±1 μA cm^{-2} at 0.1 V s^{-1} to avoid the occurrence of faradic currents. EIS was then performed over a frequency range of 50 kHz–1 Hz with logarithmic point spacing (50 points) and a 10 mV voltage amplitude. The electrochemical impedance spectra were recorded from the cathodic to the anodic potential limits in 100 mV steps.

The electrochemical measurements in the IL [BuMeIm][Tf_2N] were carried out in a commercial three-electrodes thermostatted Pyrex cell (4–5 mL), inside an argon-filled dry glovebox (oxygen concentration <0.5 ppm and water concentration <5 ppm). The activated BDD, a-CNx, GC, and Pt electrodes were used as working electrodes and a platinum mesh as a counter electrode. The reference electrode was prepared by immersing a silver wire in a 0.01 M $Ag(CF_3SO_3)$ solution in [BuMeIm][Tf_2N]. The reference solution is placed in a glass liquid junction protection tube with a fine porosity frit (from Radiometer). The silver wire was electrically connected to a 20 μF capacitor soldered to a platinum wire immersed in the IL electrolyte. All potentials are reported with respect to this reference. Under these experimental conditions, the standard potential of the redox system Fc^+/Fc measured at BDD, a-CNx, GC, and Pt electrode was found to be equal to −0.393 ± 0.001 V/silver reference electrode at all temperatures which corresponds to +0.580 V/NHE (70).

3 Results and Discussion

3.1 **Brief Survey of Circuits So Far Used for Double-Layer Data Treatment**

Analysis of the EIS diagrams to describe the capacitance behavior of the electrode/IL interface is carried out using electrical equivalent circuits (EECs). Depending on the procedure used, the circuit can be of increasing complexity which is reflected in different circuits compiled from a nonexhaustive review of the literature (Figure 1). The simpler ones are shown in (A) where the double-layer capacitance is in series with the electrolyte resistance and where sometimes a low faradic current (likely ascribable to impurities like water) is considered, leading to a charge transfer resistance R_t in parallel to the capacitance (circuit A(b)) or to a constant phase element (CPE) accounting for a capacitive dispersion (circuit A(c)) (20-23, 25, 32, 37-40). For a mere capacitance as in A(a), ac voltammetry performed at a single frequency superimposed to a scanned potential is of course totally justified. This technique was used in references 20, 25, and 37−40 even for CPE conditions, and EIS was used in the other references. More complex EECs are displayed from B to F. A rigorous analysis requires using EIS and appropriate nonlinear square fitting procedures, assuming also a relevant estimate of the error (generally taken as 1% of the modulus over the whole frequency range by most of the commercially available software) to resolve the different parameter values. Circuit B used by Pajkossy and Kolb (35) was a reminder of their previous work on Pt in aqueous solution with only one *RWC* branch to describe the slow relaxations characteristic of diffusion/adsorption processes in the compact layer (36). Circuit B was also proposed by Siinor et al (32) with a single adsorption branch and without resistance for Bi(100) and an IL containing two anions, SCN^- and BF_4^-, liable to yield significant adsorption. The treatment given in reference 34 (circuit C) fulfilled the stringent requirements of EIS analysis. For circuit D used in references 42 and 47 no details about the EIS procedure and data treatment were given. Ac voltammetry was used in reference 41 with circuit (E) containing 2 CPEs. Data treatment with circuit F (28) was done only at OCP with an error of 10%.

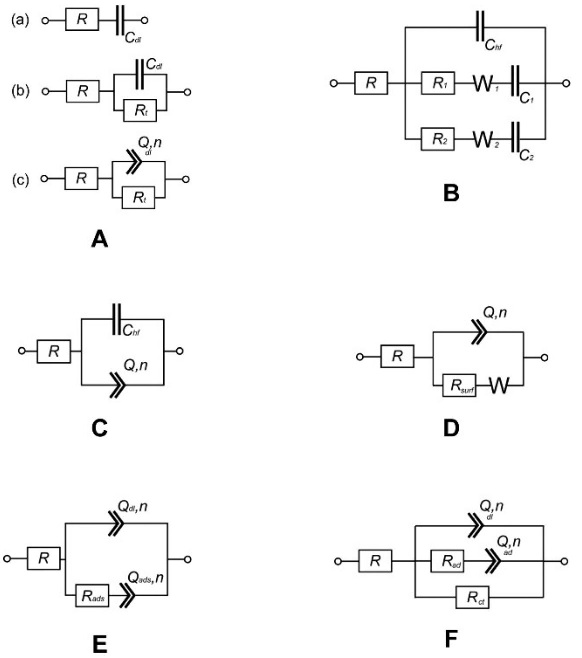

Figure 1. Different electrical equivalent circuits used for treating impedance data from several electrode/ionic liquid systems taken from the literature.

3.2 **Determination of the Potential Domain by Cyclic Voltammetry**

Cyclic voltammograms are reported in Figure SI2a-b (Supporting Information). The same scales have been used for BDD and a-CNx (Figure SI2a, Supporting Information) on one hand and for GC and Pt (Figure SI2b, Supporting Information) on the other hand, for ease of comparison. Clearly, the parasitic and capacitive currents are much lower for the first group, as already highlighted by Benchikh et al. (63) for a-CNx material, while it is widely recognized for BDD. Following the criteria defined above for the impedance measurements and the capacitance determination, the potential windows were bounded as follows: BDD (−1.9 V, +0.4 V); a-CNx (−1.9 V, +0.2 V); GC (−1.6 V, +0.2 V); Pt (−0.6 V, +0.6 V). Within these limits, the residual currents were meant to be due to impurities preexisting in the IL and not to its oxidation/reduction. It can be seen also that for all electrode materials the capacitance increases with temperature, whereas the potential window is narrowed.

3.3 **Impedance Data Analysis**

Nyquist plots(-imaginary part *I*(ω) vs *R*(ω) real part) of the impedance *Z*(ω) = *R*(ω) + *jI*(ω) display for all material conditions quasivertical lines more or less slanted, ω being the angular frequency. A better and more visual representation for such systems is to plot the admittance *Y*(ω) = 1/*Z*(ω). The admittance of a *RC* serial arrangement such as that of Figure 1A(a) gives a semicircle centered on the real axis. Four admittance diagrams corresponding to the different electrode materials are reported in Figure 2. It can be seen that none of them reproduce a perfect semicircle shape and that they all show a rather flattened one. The increasing departure from a semicircle is in the order BDD < a-CNx < Pt < GC. Actually for a-CNx, a small feature in the high-frequency (HF) range corrupts the normalization procedure, and its diagram shape is in fact close to that of BDD.

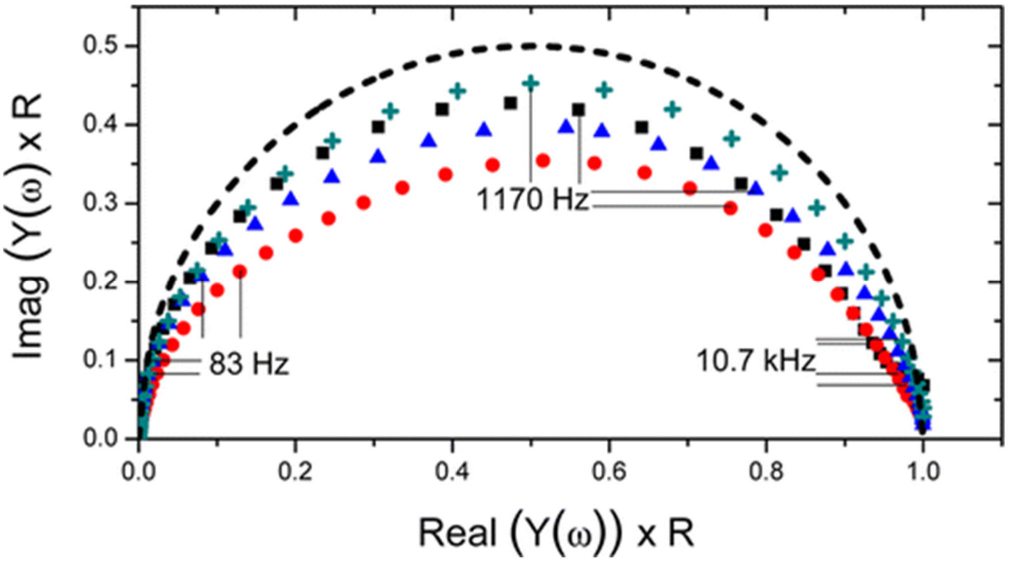

Figure 2. Admittance diagrams normalized by the real part value of the admittance at infinite frequency (Y(∞) = 1/R). (green plus) BDD (T = 50 °C, E = −0.8 V); (black square) a-CNx (T = 56 °C, E = −0.8 V); (blue triangle) Pt (T = 56 °C, E = −0.2 V); (red circle) GC (T = 56 °C, E = −0.8 V); (---) diagram corresponding to Figure 1A(a) EEC.

Among the investigated materials, it can be expected that GC and a-CNx behave as metal electrodes like Pt; i.e., there is no potential drop inside the electrode. This is true for the a-CNx films which have been elaborated in this work since the cathodic magnetron sputtering is a low-energy deposition technique producing mostly C sp^2 hybridization. Higher-energy deposition techniques at variance like a filtered cathodic vacuum arc for example produce more C sp^3hybridization where N can substitute to C in CN films and present therefore an n-type semiconductor character (71). Then for these three electrodes, the EIS response is mainly determined by the double-layer capacitance.

In agreement with the admittance diagrams of Figure 2, in a first step, a numerical analysis of experimental EIS spectra quickly showed that none of the different EECs shown in Figure 1, except F, could represent the data correctly, i.e., approach the reduced standard deviation of 1% imposed on the impedance modulus even though this value is somehow arbitrary in the absence of the knowledge of the true random error on the measured values. After proceeding by trial and error, the EEC depicted in Figure 3 was retained for the four electrodes.

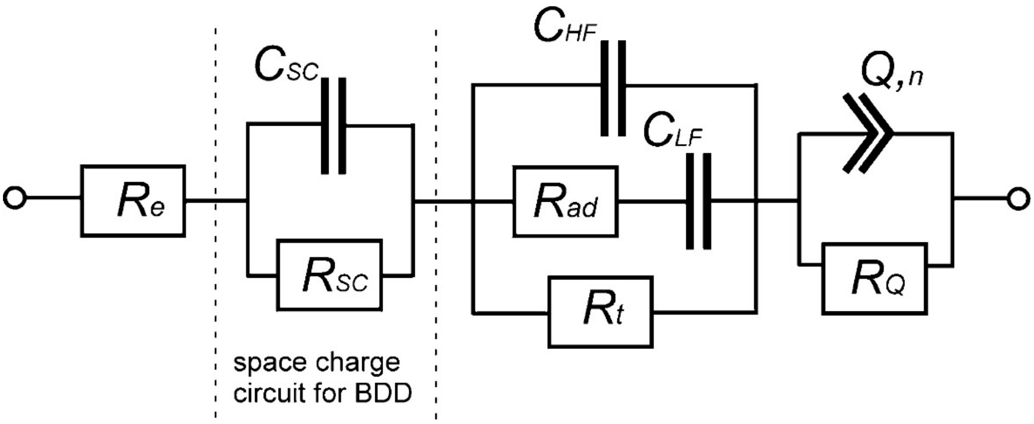

Figure 3. Equivalent electrical circuit to analyze the EIS data.

The capacitive behavior is assigned to the parallel combination of a capacitance at high frequency C_{HF} with a series (R_{ad}, C_{LF}) branch accounting for relaxation effects in the double layer. It means that the double-layer capacitance would depend on frequency, with a characteristic time $\tau_{dl} = R_{ad}C_{LF}$. The high-frequency limit is C_{HF}, and the zero-frequency limit, the so-called double-layer capacitance C_{dl}, is expressed as: $C_{dl} = C_{HF} + C_{LF}$. Within the model, C_{dl} accounts for the serial arrangement of the compact and the diffuse layer capacitances, respectively. In the circuit, R_t is added in parallel to account for some parasitic faradic current. In all cases, R_t should remain high to be consistent with the chosen potential window. The CPE element (with the usual definition of the relevant CPE impedance $Z_{CPE} = 1/(Q \times (j\omega)^{\alpha})$) was introduced as a minor but necessary contribution to improve the fit quality. It was checked that the C_{dl} central fitted values with or without this correcting circuit did not differ by more than 5%.

For the metallic or quasimetallic electrodes (Pt, GC, a-CNx), the $R_{sc}//C_{sc}$ part of the circuit introduced for a semiconducting (SC) electrode to account for a potential drop in the material due to a space charge region was of course ignored. For all the data analyzed with this circuit, the reduced standard deviation lay around 0.5%, assuming the precision on the impedance modulus to be 1%. Figures 4–6 show the variations of C_{dl} with potential for Pt, GC, and a-CNx, respectively, with an uncertainty on C_{dl} around 1%.

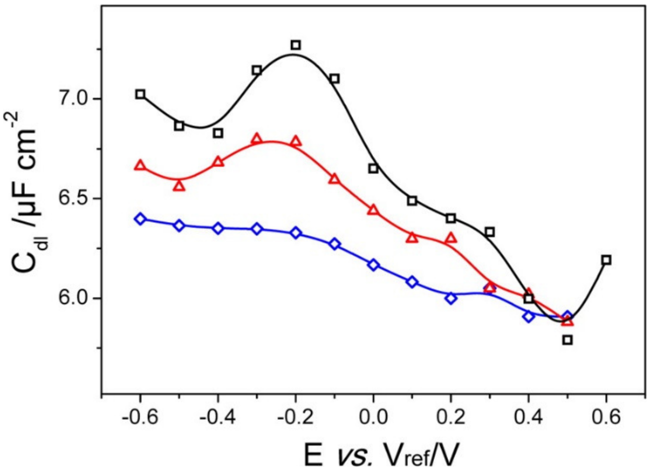

Figure 4. Double-layer capacitance for the [BuMeIm][Tf2N]/Pt interface. T = (black square) 56 °C, (red triangle) 38 °C, (blue diamond) 25 °C.

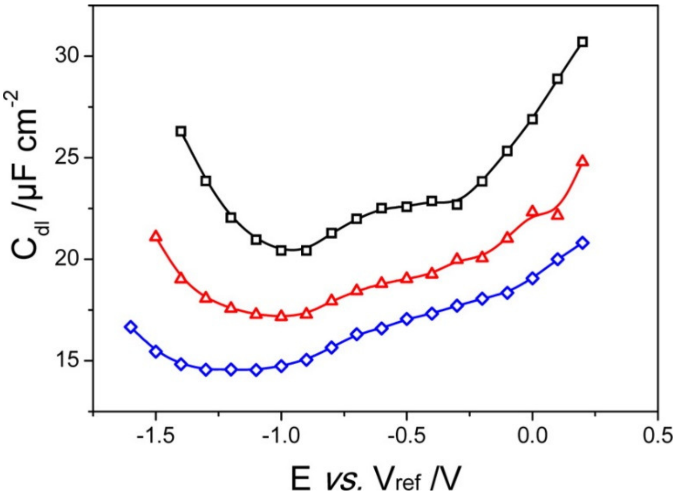

Figure 5. Double-layer capacitance for the [BuMeIm][Tf2N]/GC interface. T = (black square) 56 °C, (red triangle) 38 °C, (blue diamond) 25 °C.

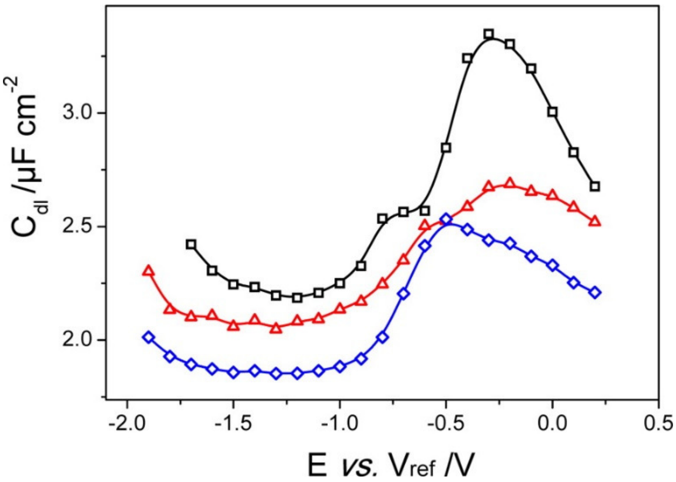

Figure 6. Double-layer capacitance for the [BuMeIm][Tf2N]/a-CNx interface. T = (black square) 56 °C, (red triangle) 38 °C, (blue diamond) 25 °C.

For Pt, a maximum of C_{dl} is observed at −0.2/–0.3 V, with a magnitude increasing with temperature from 25 to 56 °C. For GC, a general parabolic shape is observed for the $C_{dl}(E)$ curve. However, a small hump like an emerging bell shape located around −0.6 V becomes more visible with increasing temperature. For a-CNx, the $C_{dl}(E)$ curves are finely structured with a well-defined capacitance peak centered at −0.3 V. In this case, the temperature increase gradually shows an additional shoulder around −0.7 V. The modulus Q of the CPE element is generally poorly defined with uncertainties ranging from 20 to 100%. The CPE exponent α varies from 0.5 (Pt at 25 °C; a-CNx at 25, 38, 56 °C) to 0.7–0.8 (Pt at 38, 56 °C; GC at 25, 38, 56 °C), indicating some change in the transport of ions, purely diffusional or not. As expected for the potential domain studied, $R_t$takes high values between 10^5 and 10^6 Ω cm^{-2}.

From Figures 4, 5, and 6, one can put forward the occurrence of bell shaped $C_{dl}(E)$ curves for the metallic or quasimetallic electrodes investigated and the chosen IL. It must be emphasized that this conclusion is more obvious as the temperature is higher. It is also proved that C_{dl} increases with temperature in agreement with other experimental works and the predictions of theories on molten salts. There is a possible occurrence of a camel shape for a-CNx at higher temperature. This will be discussed later.

These results substantiate the predictions in the seminal work of Kornyshev (1) and the subsequent refinements (2-5) in which the theory of the double layer was treated in the frame of the lattice gas model where the volume of liquid excluded by ions is taken to be nonzero as it is in the Gouy–Chapman model for ideally dilute solutions. In particular, the main result of this analytical model is featured by a bell shape or camel shape of the double-layer capacitance vs potential curve, the maximum being close to the pzc with a parabolic shape instead of the minimum predicted in the Gouy–Chapman model. One critical ingredient is a compactness factor "γ" defined as the ratio of the bulk density of ions to the maximum possible density in the double layer. This implies the presence of voids in the system opening the possibility of increased compactness in the presence of higher electric fields, i.e., in the double layer. The possibility of a compact (or Helmholtz) layer and specific adsorption at the interface were not envisaged at the beginning, and a parabolic decrease of the total capacitance at high overpotentials due to lattice saturation was demonstrated. The bell-shape situation corresponds to $1/3 < \gamma < 1$. For $0 < \gamma < 1/3$ a camel shape is predicted, $\gamma \sim 0$ being the Gouy–Chapman case.

Later on, Fedorov and Kornyshev (5) evidenced by molecular dynamics simulations the overscreening regime, i.e., when the first layer of counterions (ions of opposite charge to that of the metal surface) exceeds the charge of the metal surface. Then, there is a second layer of co-ions followed by several layers of alternating charges until electroneutrality. The double layer is not thus "one layer thick" (48). The authors of reference 5 confirm the $C_{dl} \propto E^{-1/2}$ dependence for high E values predicted initially by Kornyshev (1) as resulting from gas-lattice saturation effects. In addition, for cations and anions of the same size, $E_{max} \sim E_{pzc}$; otherwise, the potential difference is larger as the size difference increases. Van der Waals volumes for $BuMeIm^+$ and Tf_2N^- (0.266 and 0.248 nm^3, respectively (72, 73)) would ensure here this matching condition. It was also shown that long neutral tails (like alkyl chains for imidazolium) favor camel shape and short tail the bell shape in particular because excluded volume effects and cation shape asymmetry increase the latent voids and therefore lower γ value (3, 17). For low charges, the cations are either oriented by their neutral chains or flattened by the polar head (e.g., imidazolium).

The situation is different with the BDD electrode which is a semiconducting material. A space charge region can develop inside BDD implying a distribution of the potential drop through the interface. The electrode impedance can now be represented by the complete equivalent circuit depicted in Figure 3. Two parallel resistance–capacitance circuits are in series representing the contributions of the semiconductor (SC) capacitance C_{sc} of BDD and that of the double-layer C_{dl}, respectively. As above, it was found necessary to add a parallel combination of a CPE element $Q(\alpha)$ with a resistance R_q. The SC capacitance C_{sc} is the dominant parameter of the impedance spectra allowing it to be finely determined at a precision better than 1%. Conversely the double-layer capacitance C_{dl}, as well as the CPE modulus Q, are known with a precision not better than 10–30%. Figure 7 shows the variations of C_{dl} with potential at temperatures of 25, 50, and 56 °C for potential scans from negative to positive values. A peak centered at −0.8 V progressively appears when the temperature increases.

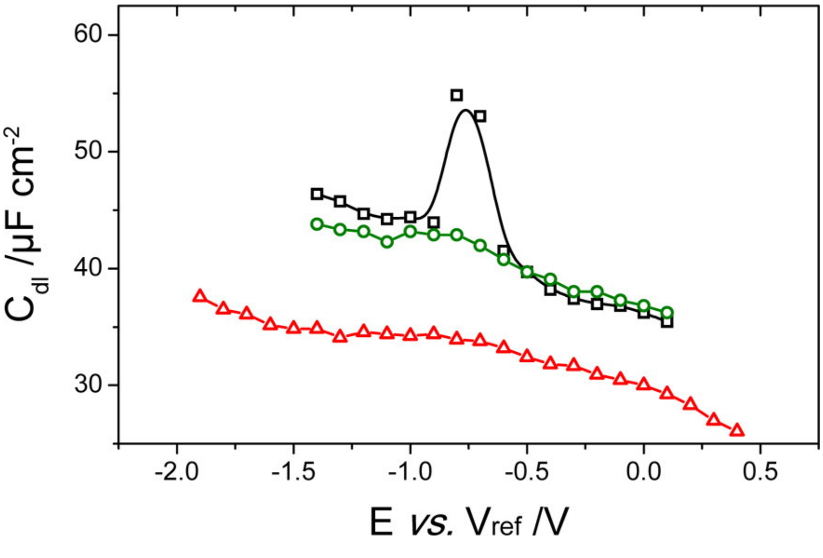

Figure 7. Double-layer capacitance for the [BuMeIm][Tf2N]/BDD interface. T = (black square) 56 °C, (green circle) 50 °C, (red triangle) 25 °C.

For BDD, more information about the interfacial behavior stems from the semiconductor capacitance C_{sc}. Figure 8 shows the variation of C_{sc} with potential in the Mott–Schottky (MS) representation, $C_{sc}^{-2}(E)$, for data sets at different temperatures between 25 and 56 °C. At 25 °C, a straight line is obtained over more than 1 V as expected for a polycrystalline semiconductor. The slope is negative, in agreement with the p type character owing to the boron doping of diamond. Its value is 0.019 cm^4 µF^{-2} V^{-1}. Considering the relative dielectric constant of diamond (74) taken as a reference for BDD to be $\varepsilon = 5.7$, it yields the doping level to be 1.3×10^{21} cm^{-3} lower than but close to the B atomic concentration given in the Experimental section ($\sim 3 \times 10^{21}$ cm^{-3}) and visible for the bulk conditions in Figure SI1 (Supporting Information). However, on the same curve it can be seen that the B concentration curve starts a slight decrease closer to the interface. In fact, it was shown earlier (66, 73) that interstitial H during synthesis and at the end of the process may actually form B–H pairing with substitutional B. This gives rise to a passivation because boron atoms do not play their role as shallow acceptors, and this corresponds to a lower doping level in the interfacial region. Another possibility would be the dependence of ε on the diamond grain size which is predicted to decrease for smaller grain sizes, which would increase the estimated doping level (75).

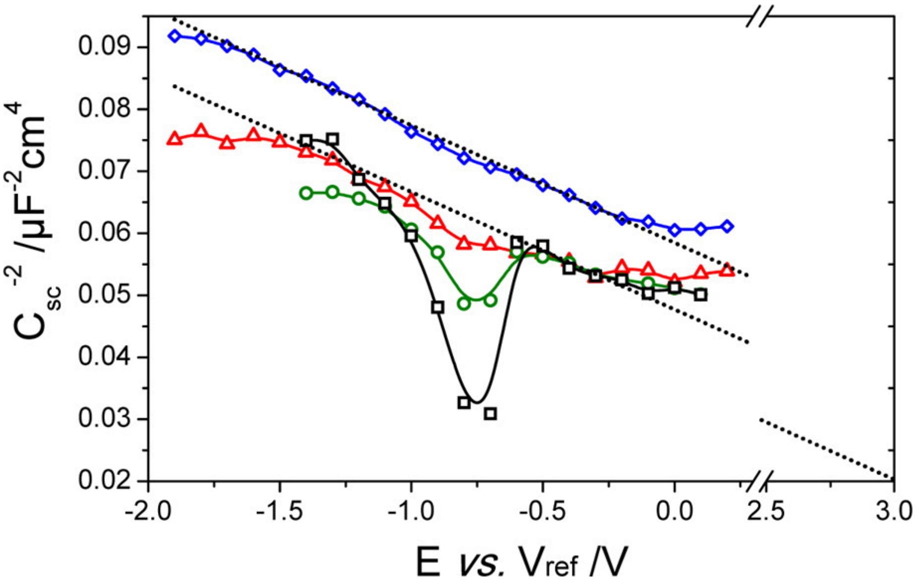

Figure 8. Mott–Schottky plots (Csc–2 vs E) for the [BuMeIm][Tf2N]/BDD interface. T= (black square) 56 °C, (green circle) 50 °C, (red triangle) 38 °C, (blue diamond) 25 °C.

A linear extrapolation at $C^{-2} = 0$ leads to a very positive value of $V_o = +3.0$ V. Such a high value was already observed by Kondo et al. for a polycrystalline BDD electrode immersed in a H_2SO_4solution and was tentatively explained by the presence of a thin dielectric layer at the diamond surface (76). When increasing the temperature, MS plots only present partial linear segments keeping the same slope but shifted more or less with respect to the curve at 25 °C taken as a reference. Additionally, between −0.6 and −1.1 V, capacitance values present a maximum, which corresponds to a deep minimum of the MS plots around −0.8 V. In terms of semiconductor electrochemistry, such a capacitance peak can be assigned to the capacitive contribution C_{ss} of surface states superimposed to that of C_{sc}. C_{ss} arises from charge relaxation effects in this potential range possibly attributed to the rearrangement of the compact ionic layer around the pzc.

At very positive potential values with respect to pzc, a compact layer of anions is formed at the BDD surface, and similarly, at very negative values, a compact layer of cations is created in the “crowding” conditions of counterions defined by Bazant et al.(2) The disturbed region around pzc would correspond to the inversion of the composition of the compact layer, from a cation-rich to anion-rich composition (“overscreening” regime).

The capacitance peak corresponds to a charge variation of $\Delta Q_{ss} \approx 0.5$–1 µC cm^{-2}, from which one can deduce a rough estimation of the surface state density as 3–6 × 10^{12} cm^{-2}, i.e., less than 1% of the total electrode surface.

It is important to note that the compact ionic layer can play a double role, as influencing the surface charge of BDD imposing its band edge position but also as a thin dielectric layer about 1 nm thick. The latter is equivalent to a capacitance C_{layer} of the order 3–5 μF cm^{-2}, in series with the SC capacitance of BDD. This series arrangement yields the measured capacitance $C_{\text{sc}}(E)$ and is responsible for the large positive value of the V_o potential. In fact, the flatband potential E_{fb}, which corresponds to pzc in the case of a semiconductor as BDD, is located in the transition zone of the MS plot, around −0.8 V. To get E_{fb} from V_o, the latter has to be corrected negatively according to the expression given by De Gryse et al (77).

$$E_{\text{fb}} = V_o - \frac{\varepsilon\varepsilon_0 q N_d}{2C_{\text{layer}}^2} = 3.0 - 3.8 = -0.8 \text{ V}$$

which is verified when taking C_{layer} = 3.5 μF cm^{-2}. This calculation is intended to point out the dramatic effect of the presence of a compact ionic layer on the MS plots. Conversely, the positive shift of MS plots is a strong indication in favor of the existence of an ionic compact layer in each potential domain, anodic and cathodic.

The well-defined capacitance peak in the case of the a-CNx electrode can be tentatively compared to the predictions of the Kornyshev theory about the diffuse layer capacitance established at the interface between an ionic liquid and an electrode (1). In the case of a-CNx electrode, a comparison seems feasible if two points are taken into consideration. The first one is to consider that a compact layer is present at the interface characterized by a capacitance C_H of the order of a few μF cm^{-2}, as seen previously in the case of the BDD electrode. The second point is a consequence of the first one; i.e., a potential distribution has to be taken into account at the interface, due to the series arrangement between the capacitances C_H and C_{dif} of the compact and diffuse layers. C_H was assigned a sigmoid profile with different anodic and cathodic plateaus far from the pzc

$$C_H = C_H^{\text{anod}} + \frac{C_H^{\text{cath}} - C_H^{\text{anod}}}{1 + \exp \lambda(E - E_{1/2})}$$

λ^{-1} represents the main potential domain where C_H varies from the anodic to cathodic plateaus. $E_{1/2}$ marks in the simulation the switching potential between the anodic and cathodic domains for the different types of cation adsorption. However, it must be emphasized that $E_{1/2}$ does not necessarily correspond to the pzc.

The diffuse layer capacitance C_{dif} was taken from the work of Kornyshev (1)

$$C_{\text{dif}} = C_0 \frac{\cosh(u/2)}{1 + 2\gamma(\sinh(u/2))^2} \sqrt{\frac{2\gamma(\sinh(u/2))^2}{\ln[1 + 2\gamma(\sinh(u/2))^2]}}$$

With

$$\gamma = \gamma_a + \frac{\gamma_c - \gamma_a}{1 + \exp(u)}$$

γ_a and γ_c are the anodic and cathodic packing contributions, respectively.

In this formula, u was a reduced potential seen by the diffuse layer considering that the total potential drop ΔE referring to the pzc at the interface occurred in the diffuse layer and

$$u = \frac{e\Delta E}{k_B T}$$

In fact, the potential drop across the diffuse layer is only a fraction of the total applied potential due to the presence of the compact layer. As an approximation, we assumed that the potential drop was shared between the compact and diffuse layers according to the respective capacitance values which led to the following definition of u variations

$$du = \frac{e dE}{k_B T} \times \frac{C_H}{C_H + C_{\text{dif}}}$$

On this basis, it was possible to build the double-layer capacitance curve $C_{dl}(E)$ numerically by iterative increments of the applied potential dE and extract the different parameters (see the Supporting Information for the details of the procedure). The first try was done with the data from the a-CNx electrode at 56 °C which displayed the most obvious existence of a camel shape curve. This guess was validated by the small γ_a and γ_c values consistent with this shape.

This finding led us to apply the same procedure to the other three electrode materials at the highest temperature where the effects are more visible and also to a-CNx at the lower temperatures. The C_{dl} curves in Figure 9 show that a reasonable agreement is reached in potential domains which are meant to correspond to the respective pzc's. The relevant parameter values are reported in Table 1.

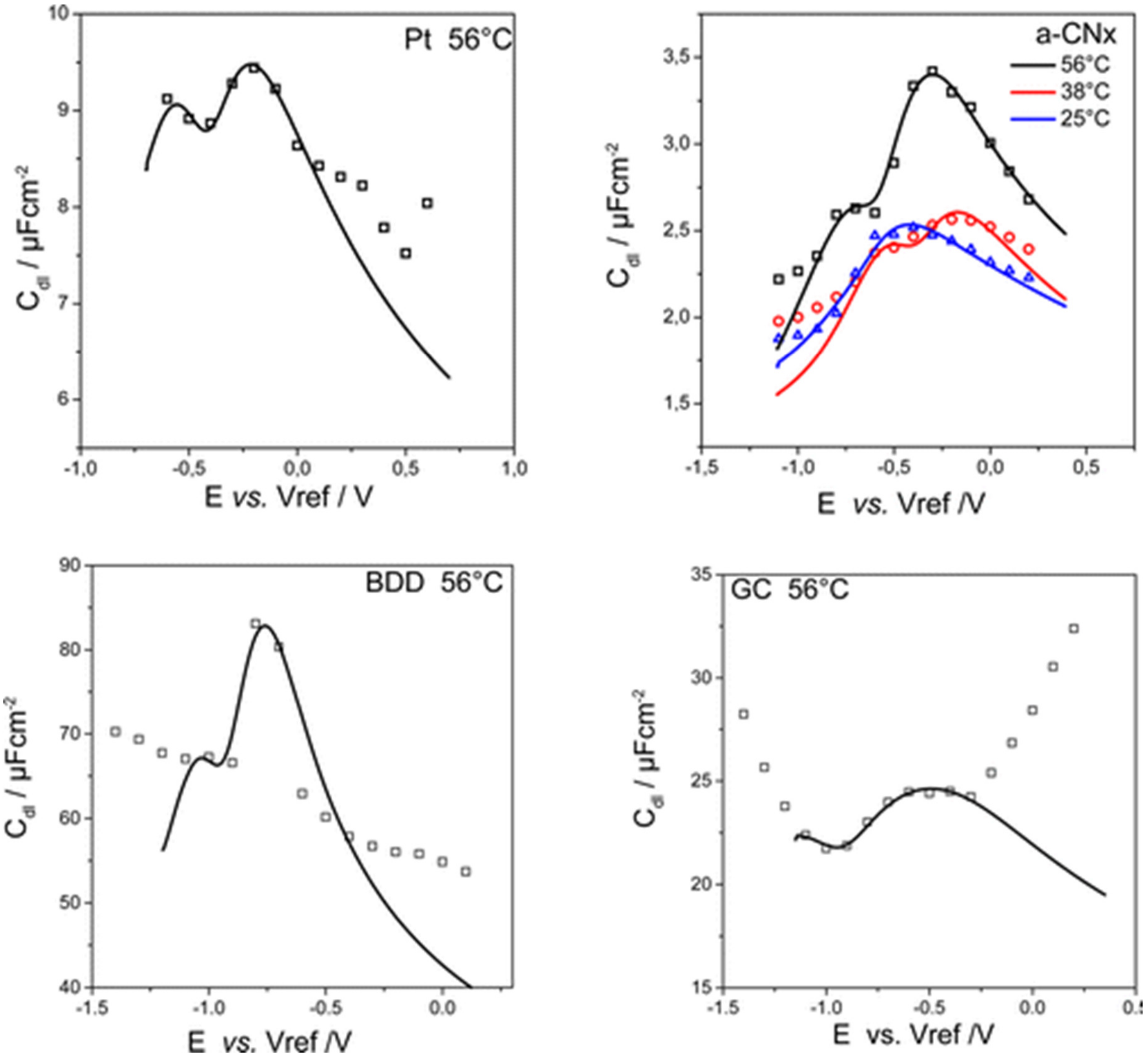

Figure 9. Simulated (full lines) and experimental (symbols) Cdl values vs potential assuming Cdl as the sum of a compact (CH) and a diffuse (Cdif) capacitance. CHand Cdif are defined by eqs 2 and 3, respectively. Materials and temperature conditions are indicated in the figures.

Table 1. Fitted Values of the Parameters in Equations 2–4

	C_0	C_H^{anod}	C_H^{cath}	$C_H^{anod} - C_H^{cath}$	$E_{1/2}$	λ^{-1}				C_0	C_H^{anod}
	μF cm^{-2}	μF cm^{-2}	μF cm^{-2}	μF cm^{-2}	V/ref	V	γ_a	γ_c		μF cm^{-2}	μF cm^{-2}
a-CNx									a-CNx		
56 °C	7.90	5.40	1.10	4.30	−0.81	0.27	0.10	0.10	56 °C	7.90	5.40
38 °C	8.00	3.50	2.10	1.40	−0.80	0.16	0.12	0.19	38 °C	8.00	3.50
25 °C	10.0	3.15	1.55	1.60	−0.90	0.15	0.10	0.22	25 °C	10.0	3.15
DD									DD		
56 °C	145	190	108	82	−0.80	0.10	0.14	0.20	56 °C	145	190
GC									GC		
56 °C	76.0	38.0	30.2	7.80	−0.50	0.12	0.11	0.20	56 °C	76.0	38.0

In spite of the unfavorable conditions for quantitative determination of the parameters (too few capacitance values with respect to the parameters number), general trends can emerge:

- The diffuse layer capacitance is camel shaped (see Figure 10 for the C_H and C_{dif} elementary curves) which is consistent with the fact that γ, according to eq 4, is bounded by γ_a or γ_c which means in this case 0.23, lower than the 0.33 value predicted by Kornyshev (1) for C_{dif} to adopt this shape.

- It must be emphasized that the γ_a or γ_c values (about 0.1 and 0.2, respectively) are slightly depending on the electrode material nature (except for a-CNx at 56 °C) as they are rather determined by the chemical and structural characteristics of the anions and cations.

- C_H^{cath} is systematically lower than C_H^{anod}, which, for cathodic overpotentials, could validate an adsorption of the cation by the alkyl tail and/or a contribution of the anion due to its smaller size.

- $E_{1/2}$ marking the switch over from C_H^{cath} to C_H^{anod} could correspond to the pzc. It is worth mentioning that a-CNx and BDD show a close value around −0.8 V, and though the GC value is about −0.5 V, this would indicate that it stems from the common carbon nature of those materials. The switchover range of the order of λ^{-1} does not exceed 0.27 V.

- The increase of C_{dl} with temperature is confirmed.

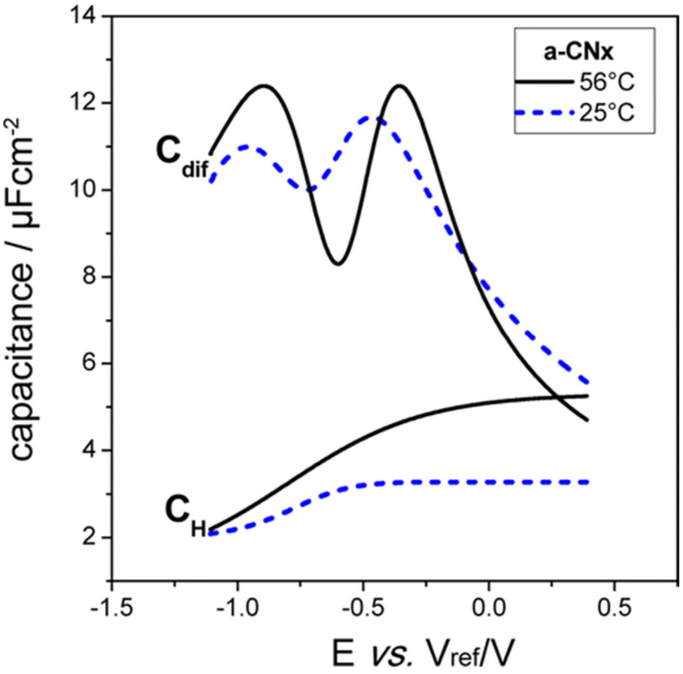

Figure 10. Compact (CH) and diffuse (Cdif) capacitances defined by eqs 2 and 3, respectively, vs potential for the system a-CNx at 25 and 56 °C.

4 Conclusions

Characterization of the double layer of [BuMeIm][Tf$_2$N] ionic liquid has been carried out for four different types of electrode materials: one metallic (Pt) and three carbon materials having different conductivity properties, from a highly conductive (GC), mean conductivity (a-CNx), and semiconducting (BDD) though with a quasi metallic character.

It was found that for those four materials the same equivalent electrical circuit could be used with a good confidence to account for the experimental results.

- The BDD material only needed the use of a specific additional circuit involving the capacitance of the space charge within the material: Mott–Schottky plots allowed confirming the p-type SC characteristics and the doping level which closely corresponded to the boron amount purposely introduced during the film synthesis.

- The double layer, composed of the serial arrangement of a compact layer (equivalent to the Helmholtz one in aqueous solvent) and the diffuse layer one, was a true capacitance and not a CPE, which involves only a single time constant for the reorganization of the double layer, conversely to the presence of a CPE appearing in some other electrical circuits proposed in the literature. It was paralleled by a serial arrangement of a resistance and a capacitance allowing for low-frequency relaxation involving rearrangements in the compact layer.

- A tentative splitting of the double-layer capacitance into the compact and diffuse capacitances showed that the potential dependence of the latter one displayed a camel shape in agreement with the prediction of the Kornyshev theory for low values of the packing parameter γ.

- This work points out the critical role of the compact layer in determining the observable profile of the double-layer capacitance in ionic liquids. The electronic characteristics of the electrode material are not the only determining parameter for the compact layer capacitance values considering the ranking (BDD > GC > Pt > a-CNx).

- Double-layer capacitances increased with temperature, following a trend similar to what is observed in molten salts. For ionic liquids, the origin could be the increasing agitation with temperature weakening several forces able to maintain associations between the ions (Coulombic forces, Van der Waals forces, H bonding).

Supporting Information

SIMS profile of the BDD electrode; cyclic voltammograms of [BuMeIm][Tf$_2$N] on BDD, a-CNx, GC, and Pt electrodes; procedure used for simulation of the double-layer capacitance. This material is available free of charge via the Internet at http://pubs.acs.org.

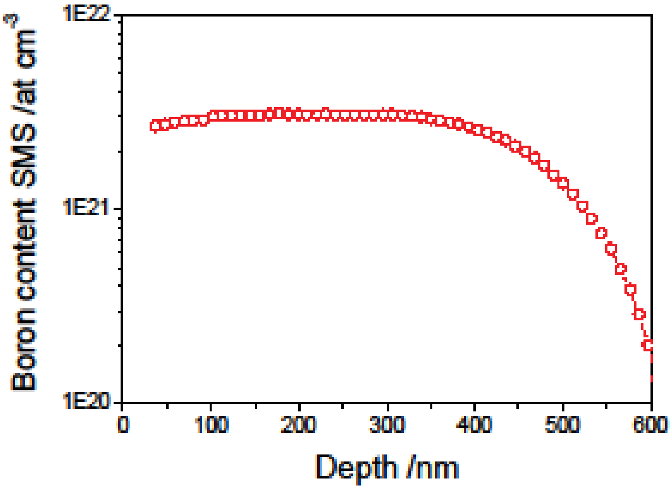

Figure SI 1. SIMS profile of the BDD electrode

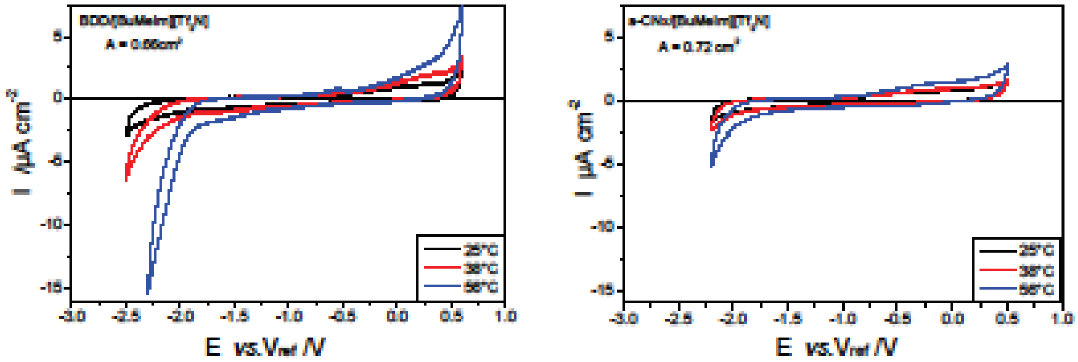

Figure SI 2a. Cyclic voltammograms of [BuMeIm][Tf$_2$N] on BDD (left) or a-CNx (right) electrodes. Scan rate 100 mV s^{-1}

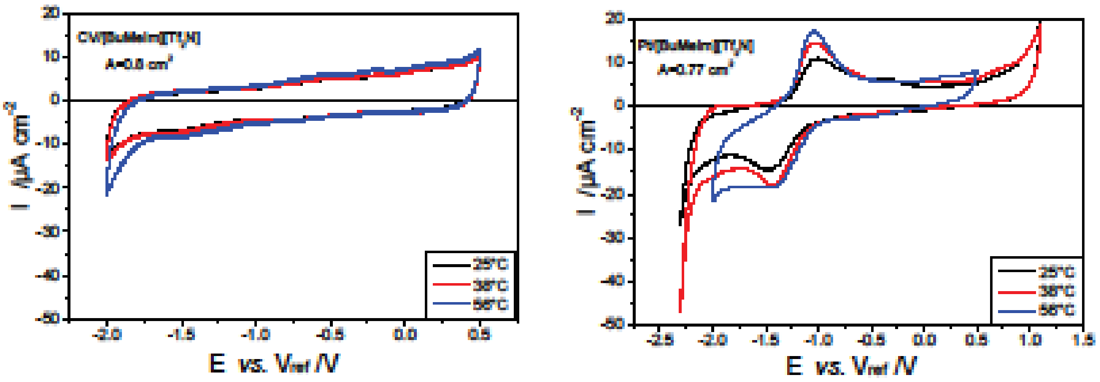

Figure SI 2b. Cyclic voltammograms of [BuMeIm][Tf$_2$N] on GC (left) or Pt (right) electrodes. Scan rate 100 mV s^{-1}

Simulation of the double layer capacitance C_{dl} at an ionic liquid/electrode interface

Eight parameters are involved in the simulation of the interfacial capacitance C_{dl} *vs.* electrode potential E, 4 for the diffuse layer, 4 for the compact layer. These are:

Diffuse layer:	Udl_0	(Volt)	
	C_o	(µF cm^{-2})	(Eq.3)
	γ_a		(Eq.4)
	γ_c		(Eq.4)
Compact layer:	C_H^{anod}	(µF cm^{-2})	(Eq.2)
	C_H^{cath}	(µF cm^{-2})	(Eq.2)
	$E_{1/2}$	V (/ref)	(Eq.2)
	λ	V^{-1}	(Eq.2)

Their values have to be fixed before beginning the calculation. They are defined in the text, except Udl_0 which represents the initial value to be given to the potential drop through the diffuse layer. The capacitance voltage divider (du/dE) is defined by Eq.6 in the text.

Initializing the variables at an arbitrary starting potential E_0:

$$E_0,\ Udl_0,\ u_0 = e.Udl_0/k_BT,\ C_{H0},\ C_{dif0},\ \left(du/dE\right)_0 = \frac{e}{k_BT}\frac{C_{H0}}{C_{H0}+C_{dif0}},\ C_{dl0} = \frac{C_{H0}C_{dif0}}{C_{H0}+C_{dif0}}$$

The $C_{dl}(E)$ curve is then constructed step by step incrementing the applied potential by dE, calculating the state i+1 from the state i according to:

$$E_{i+1} = E_i + dE$$

$$Udl_{i+1} = Udl_i + \left(\frac{du}{dE}\right)_i dE$$

$$\left(\frac{du}{dE}\right)_{i+1} = \left(\frac{C_H}{C_H + C_{dif}}\right)_i$$

$$(C_H)_{i+1} = C_H^{anod} + \frac{C_H^{cath} - C_H^{anod}}{1 + \exp\lambda(E_i - E_{1/2})}$$

$$u_{i+1} = \frac{e \cdot Udl_i}{k_B T}$$

$$\gamma_{i+1} = \gamma_a + \frac{\gamma_c - \gamma_a}{1 + \exp(u_i)}$$

$$(C_{dif})_{i+1} = C_0 \frac{\cosh(u_i/2)}{1 + 2\gamma_i(\sinh(u_i/2))^2} \sqrt{\frac{2\gamma_i(\sinh(u_i/2))^2}{\ln\left[1 + 2\gamma_i(\sinh(u_i/2))^2\right]}}$$

$$(C_{dl})_{i+1} = \left(\frac{C_H C_{dif}}{C_H + C_{dif}}\right)_i$$

The $C_{dl}(E)$ curve which was built using Mathcad 7 software (from Mathsoft) using this procedure was compared to the experimental one, and the 8 adjustable parameters to be modified up to obtain a satisfying representation of the data to the naked eye.

Acknowledgment

The authors declare no competing financial interest.
The authors thank the national research programs PARIS and Needs for their financial support.

References

This article references 77 other publications.

1. Kornyshev, A. A. Double-Layer in Ionic Liquids: Paradigm Change? *J. Phys. Chem. B* **2007**, 111, 5545–5557

2. Bazant, M. Z.; Storey, B. D.; Kornyshev, A. A. Double Layer in Ionic Liquids: Overscreening versus Crowding *Phys. Rev. Lett.* **2011**, 106, 046102

3. Fedorov, M. V.; Georgi, N.; Kornyshev, A. A. Double layer in ionic liquids: The nature of the camel shape of capacitance *Electrochem. Commun.* **2010**, 12, 296– 299

4. Fedorov, M. V.; Kornyshev, A. A. Ionic Liquid Near a Charged Wall: Structure and Capacitance of Electrical Double Layer *J. Phys. Chem. B* **2008**, 112, 11868– 11872

5. Fedorov, M. V.; Kornyshev, A. A. Towards understanding the structure and capacitance of electrical double layer in ionic liquids *Electrochim. Acta* **2008**, 53, 6835– 6840

6. Georgi, N.; Kornyshev, A. A.; Fedorov, M. V. The anatomy of the double layer and capacitance in ionic liquids with anisotropic ions: Electrostriction vs. lattice saturation *J. Electroanal. Chem.* **2010**, 649, 261–267

7. Henderson, D.; Wu, J. Electrochemical Properties of the Double Layer of an Ionic Liquid Using a Dimer Model Electrolyte and Density Functional Theory *J. Phys. Chem. B* **2012**, 116, 2520– 2525

8. Vatamanu, J.; Borodin, O.; Smith, G. D. Molecular Insights into the Potential and Temperature Dependences of the Differential Capacitance of a Room-Temperature Ionic Liquid at Graphite Electrodes *J. Am. Chem. Soc.* **2010**, 132, 14825– 14833

9. Vatamanu, J.; Borodin, O.; Bedrov, D.; Smith, G. D. Molecular Dynamics Simulation Study of the Interfacial Structure and Differential Capacitance of Alkylimidazolium Bis(trifluoromethanesulfonyl)imide [Cnmim][TFSI] Ionic Liquids at Graphite Electrodes *J. Phys. Chem. C* **2012**, 116, 7940– 7951

10. Lamperski, S.; Outhwaite, C. W.; Bhuiyan, L. B. The Electric Double-Layer Differential Capacitance at and near Zero Surface Charge for a Restricted Primitive Model Electrolyte *J. Phys. Chem. B* **2009**, 113, 8925–8929

11. Loth, M. S.; Skinner, B.; Shklovskii, B. I. Anomalously large capacitance of an ionic liquid described by the restricted primitive model *Phys. Rev. E* **2010**, 82, 056102

12. Outhwaite, C. W.; Lamperski, S.; Bhuiyan, L. B. Influence of electrode polarization on the capacitance of an electric double layer at and around zero surface charge *Mol. Phys.* **2011**, 109, 21– 26

13. Oldham, K. B. A Gouy–Chapman–Stern model of the double layer at a (metal)/(ionic liquid) interface *J. Electroanal. Chem.* **2008**, 613, 131– 138

14. Liu, L.; Li, S.; Cao, Z.; Peng, Y.; Li, G.; Yan, T.; Gao, X.-P. Well-Ordered Structure at Ionic Liquid/Rutile (110) Interface *J. Phys. Chem. C* **2007**, 111, 12161– 12164

15. Feng, G.; Jiang, D.-E.; Cummings, P. T. Curvature Effect on the Capacitance of Electric Double Layers at Ionic Liquid/Onion-Like Carbon Interfaces *J. Chem. Theory Comput.* **2012**, 8, 1058– 1063

16. Kislenko, S. A.; Samoylov, I. S.; Amirov, R. H. Molecular dynamics simulation of the electrochemical interface between a graphite surface and the ionic liquid [BMIM][PF_6] *Phys. Chem. Chem. Phys.* **2009**, 11,5584– 5590

17. Lauw, Y.; Horne, M. D.; Rodopoulos, T.; Nelson, A.; Leermakers, F. A. M. Electrical Double-Layer Capacitance in Room Temperature Ionic Liquids: Ion-Size and Specific Adsorption Effects *J. Phys. Chem. B***2010**, 114, 11149– 11154

18. Lauw, Y.; Horne, M. D.; Rodopoulos, T.; Leermakers, F. A. M. Room-Temperature Ionic Liquids: Excluded Volume and Ion Polarizability Effects in the Electrical Double-Layer Structure and Capacitance *Phys. Rev. Lett.* **2009**, 103, 117801(4)

19. Alam, M. T.; Islam, M. M.; Okajima, T.; Ohsaka, T. Capacitance Measurements in a Series of Room-Temperature Ionic Liquids at Glassy Carbon and Gold Electrode Interfaces *J. Phys. Chem. C* **2008**, 112,16600– 16608
20. Islam, M. M.; Alam, M. T.; Okajima, T.; Ohsaka, T. Electrical Double Layer Structure in Ionic Liquids: An Understanding of the Unusual Capacitance–Potential Curve at a Nonmetallic Electrode *J. Phys. Chem. C***2009**, 113, 3386– 3389
21. Lockett, V.; Sedev, R.; Ralston, J.; Horne, M.; Rodopoulos, T. Differential Capacitance of the Electrical Double Layer in Imidazolium-Based Ionic Liquids: Influence of Potential, Cation Size, and Temperature *J. Phys. Chem. C* **2008**, 112, 7486– 7495
22. Pauliukaite, R.; Doherty, A. P.; Murnaghan, K. D.; Brett, C. M. A. Characterisation and application of carbon film electrodes in room temperature ionic liquid media *J. Electroanal. Chem.* **2008**, 616, 14– 26
23. Silva, F.; Gornes, C.; Figueiredo, M.; Costa, R.; Martins, A.; Pereira, C. M. The electrical double layer at the [BMIM][PF_6] ionic liquid/electrode interface – Effect of temperature on the differential capacitance *J. Electroanal. Chem.* **2008**, 622, 153– 160
24. Zheng, J. P.; Goonetilleke, P. C.; Pettit, C. M.; Roy, D. Probing the electrochemical double layer of an ionic liquid using voltammetry and impedance spectroscopy: A comparative study of carbon nanotube and glassy carbon electrodes in $[EMIM]^+[EtSO_4]^-$ *Talanta* **2010**, 81, 1045– 1055
25. Islam, M. M.; Alam, M. T.; Ohsaka, T. Electrical Double-Layer Structure in Ionic Liquids: A Corroboration of the Theoretical Model by Experimental Results *J. Phys. Chem. C* **2008**, 112, 16568– 16574
26. Katkevics, J.; Viksna, A.; Zicmanis, A.; Vaivars, G. Electrical impedance spectroscopy of ionic liquid 1-ethyl-3-methylimidazolium methanesulfonate (ECOENG 110) *Solid State Ionics* **2011**, 188, 114– 117
27. Druschler, M.; Huber, B.; Passerini, S.; Roling, B. Hysteresis Effects in the Potential-Dependent Double Layer Capacitance of Room Temperature Ionic Liquids at a Polycrystalline Platinum Interface *J. Phys. Chem. C* **2010**, 114, 3614– 3617
28. Moganty, S. S.; Baltus, R. E.; Roy, D. Electrochemical windows and impedance characteristics of $[Bmim^+][BF_4^-]$ and $[Bdmim^+][BF_4^-]$ ionic liquids at the surfaces of Au, Pt, Ta and glassy carbon electrodes *Chem. Phys. Lett.* **2009**, 483, 90– 94
29. Roling, B.; Drueschler, M.; Huber, B. Slow and fast capacitive process taking place at the ionic liquid/electrode interface *Faraday Discuss.* **2012**, 154, 303– 311
30. Alam, M. T.; Islam, M. M.; Okajima, T.; Ohsaka, T. Measurements of Differential Capacitance at Mercury/Room-Temperature Ionic Liquids Interfaces *J. Phys. Chem. C* **2007**, 111, 18326– 18333
31. Costa, R.; Pereira, C. M.; Silva, F. Double layer in room temperature ionic liquids: influence of temperature and ionic size on the differential capacitance and electrocapillary curves *Phys. Chem. Chem. Phys.* **2010**,12, 11125– 11132

32. Siinor, L.; Lust, K.; Lust, E. Influence of anion composition and size on the double layer capacitance for Bi(111)/room temperature ionic liquid interface *Electrochem. Commun.* **2010**, 12, 1058– 1061

33. Siinor, L.; Lust, K.; Lust, E. Electrical Double Layer Capacitance at Bi(111)/1 -Ethyl-3-methylimidazolium Tetrafluoroborate Interface as a Function of the Electrode Potential Physical and Analytical Electrochemistry*J. Electrochem. Soc.* **2010**, 157, F83– F87

34. Gnahm, M.; Pajkossy, T.; Kolb, D. M. The interface between Au(111) and an ionic liquid *Electrochim. Acta***2010**, 55, 6212– 6217

35. Pajkossy, T.; Kolb, D. M. The interfacial capacitance of Au(100) in an ionic liquid, 1-butyl-3-methyl-imidazolium hexafluorophosphate *Electrochem. Commun.* **2011**, 13, 284– 286

36. Pajkossy, T.; Kolb, D. M. Anion-adsorption-related frequency-dependent double layer capacitance of the platinum-group metals in the double layer region *Electrochim. Acta* **2008**, 53, 7403– 7409

37. Su, Y.-Z.; Fu, Y.-C.; Yan, J.-W.; Chen, Z.-B.; Mao, B.-W. Double Layer of Au(100)/Ionic Liquid Interface and Its Stability in Imidazolium-Based Ionic Liquids *Angew. Chem., Int. Ed.* **2009**, 48, 5148– 5151

38. Lockett, V.; Horne, M.; Sedev, R.; Rodopoulos, T.; Ralston, J. Differential capacitance of the double layer at the electrode/ionic liquids interface *Phys. Chem. Chem. Phys.* **2010**, 12, 12499– 12512

39. Alam, M. T.; Islam, M. M.; Okajima, T.; Ohsaka, T. Measurements of differential capacitance in room temperature ionic liquid at mercury, glassy carbon and gold electrode interfaces *Electrochem. Commun.***2007**, 9, 2370– 2374

40. Alam, M. T.; Islam, M.; Okajima, T.; Ohsaka, T. Ionic Liquid Structure Dependent Electrical Double Layer at the Mercury Interface *J. Phys. Chem. C* **2008**, 112, 2601– 2606

41. Gore, T. R.; Bond, T.; Zhang, W.; Scott, R. W. J.; Burgess, I. J. Hysteresis in the measurement of double-layer capacitance at the gold–ionic liquid interface *Electrochem. Commun.* **2010**, 12, 1340– 1344

42. Baldelli, S. Surface Structure at the Ionic Liquid–Electrified Metal Interface *Acc. Chem. Res.* **2008**, 41, 421–431

43. Atkin, R.; Borisenko, N.; Drueschler, M.; El Abedin, S. Z.; Endres, F.; Hayes, R.; Huber, B.; Roling, B. An in situ STM/AFM and impedance spectroscopy study of the extremely pure 1-butyl-1-methylpyrrolidinium tris(pentafluoroethyl)trifluorophosphate/Au(111) interface: potential dependent solvation layers and the herringbone reconstruction *Phys. Chem. Chem. Phys.* **2011**, 13, 6849– 6857

44. Gnahm, M.; Mueller, C.; Repanszki, R.; Pajkossy, T.; Kolb, D. M. The interface between Au(100) and 1-butyl-3-methyl-imidazolium-hexafluorophosphate *Phys. Chem. Chem. Phys.* **2011**, 13, 11627–11633

45. Aliaga, C.; Baldelli, S. Sum Frequency Generation Spectroscopy and Double-Layer Capacitance Studies of the 1-Butyl-3-Methylimidazolium Dicyanamide–Platinum Interface *J. Phys. Chem. B* **2006**, 110, 18481–18491

46. Hurth, C.; Li, C.; Bard, A. J. Direct Probing of Electrical Double Layers by Scanning Electrochemical Potential Microscopy *J. Phys. Chem. C* **2007**, 111, 4620– 4627

47. Baldelli, S. Probing Electric Fields at the Ionic Liquid–Electrode Interface Using Sum Frequency Generation Spectroscopy and Electrochemistry *J. Phys. Chem. B* **2005**, 109, 13049– 13051

48. Su, Y.; Yan, J.; Li, M.; Zhang, M.; Mao, B. Electric Double Layer of Au(100)/Imidazolium-Based Ionic Liquids Interface: Effect of Cation Size *J. Phys. Chem. C* **2013**, 117, 205– 212

49. Welton, T. Room-Temperature Ionic Liquids. Solvents for Synthesis and Catalysis *Chem. Rev.* **1999**, 99,2071– 2084

50. Buzzeo, M. C.; Evans, R. G.; Compton, R. G. Non-Haloaluminate Room-Temperature Ionic Liquids in Electrochemistry - A Review *ChemPhysChem* **2004**, 5, 1106– 1120

51. Armand, M.; Endres, F.; MacFarlane, D. R.; Ohno, H.; Scrosati, B. Ionic-liquid materials for the electrochemical challenges of the future *Nat. Mater.* **2009**, 8, 621– 629

52. Galinski, M.; Lewandowski, A.; Stepniak, I. Ionic liquids as electrolytes *Electrochim. Acta* **2006**, 51, 5567–5580

53. Macfarlane, D. R.; Forsyth, M.; Howlett, P. C.; Pringle, J. M.; Sun, J.; Annat, G.; Neil, W.; Izgorodina, E. I.Ionic Liquids in Electrochemical Devices and Processes: Managing Interfacial Electrochemistry *Acc. Chem. Res.* **2007**, 40, 1165– 1173

54. Su, Y.-Z.; Fu, Y.-C.; Wei, Y.-M.; Yan, J.-W.; Mao, B.-W. The Electrode/Ionic Liquid Interface: Electric Double Layer and Metal Electrodeposition *ChemPhysChem* **2010**, 11, 2764– 2778

55. Lu, W.; Qu, L.; Henry, K.; Dai, L. High performance electrochemical capacitors from aligned carbon nanotube electrodes and ionic liquid electrolytes *J. Power Sources* **2009**, 189, 1270– 1277

56. Xu, B.; Wu, F.; Chen, R.; Cao, G.; Chen, S.; Yang, Y. Mesoporous activated carbon fiber as electrode material for high-performance electrochemical double layer capacitors with ionic liquid electrolyte *J. Power Sources* **2010**, 195, 2118– 2124

57. Frackowiak, E.; Lota, G.; Machnikowski, J.; Vix-Guterl, C.; Béguin, F. Optimisation of supercapacitors using carbons with controlled nanotexture and nitrogen content *Electrochim. Acta* **2006**, 51, 2209–2214

58. Cachet, H.; Deslouis, C.; Chouiki, M.; Saidani, B.; Conway, N. M. J.; Godet, C. Electrochemistry of Nitrogen-Incorporated Hydrogenated Amorphous Carbon Films *J. Electrochem. Soc.* **2002**, 149, E233–E241

59. Lagrini, A.; Deslouis, C.; Cachet, H.; Benlahsen, M.; Charvet, S. Elaboration and electrochemical characterization of nitrogenated amorphous carbon films *Electrochem. Commun.* **2004**, 6, 245–248

60. Lagrini, A.; Charvet, S.; Benlahsen, M.; Debiemme-Chouvy, C.; Deslouis, C.; Cachet, H. Microstructure and electronic investigations of carbon nitride films deposited by RF magnetron sputtering *Thin Solid Films* **2005**,482, 41– 44

61. Cachet, H.; Debiemme-Chouvy, C.; Deslouis, C.; Lagrini, A.; Vivier, V.; Benlahsen, M.; Charvet, S.Improvement and characterization of the electrochemical reactivity of amorphous carbon nitride electrodes*Electrochem. Commun.* **2005**, 7, 496– 499

62. Cachet, H.; Debiemme-Chouvy, C.; Deslouis, C.; Lagrini, A.; Vivier, V. Correlation between electrochemical reactivity and surface chemistry of amorphous carbon nitride films *Surf. Interfaces Anal* **2006**, 38, 719–722

63. Benchikh, A.; Debiemme-Chouvy, C.; Cachet, H.; Pailleret, A.; Saidani, B.; Beaunier, L.; Berger, M. H.;Deslouis, C. Influence of electrochemical pre-treatment on highly reactive carbon nitride thin films deposited on stainless steel for electrochemical applications *Electrochim. Acta* **2012**, 75, 131– 138

64. Vanhove, E.; de Sanoit, J.; Arnault, J. C.; Saada, S.; Mer, C.; Mailley, P.; Bergonzo, P.; Nesladek, M.Stability of H-terminated BDD electrodes: an insight into the influence of the surface preparation *Physica Status Solidi A* **2007**, 204, 2931– 2939

65. Tamiasso-Martinhon, P.; Cachet, H.; Debiemme-Chouvy, C.; Deslouis, C. Thin films of amorphous nitrogenated carbon a-CN$_x$: Electron transfer and surface reactivity *Electrochim. Acta* **2008**, 53, 5752–5759

66. Vanhove, E.; de Sanoit, J.; Mailley, P.; Pinault, M.-A.; Jomard, F.; Bergonzo, P. High reactivity and stability of diamond electrodes: The influence of the B-doping concentration *Physica Status Solidi A* **2009**, 206, 2063–2069

67. Deslouis, C.; de Sanoit, J.; Saada, S.; Mer, C.; Pailleret, A.; Cachet, H.; Bergonzo, P. Electrochemical behaviour of (111) B-Doped Polycrystalline Diamond: Morphology/surface conductivity/activity assessed by EIS and CS-AFM *Diamond Relat. Mater.* **2011**, 20, 1– 10

68. Kiran, R.; Scorsone, E.; de Sanoit, J.; Arnault, J. C.; Mailley, P.; Bergonzo, P. Boron Doped Diamond Electrodes for Direct Measurement in Biological Fluids: An In Situ Regeneration Approach *J. Electrochem. Soc.* **2013**, 160, H67– H73

69. Kiran, R.; de Sanoit, J.; Scorsone, E. Patent application N° 11 51341 (**2011**) .

70. Ba, B.; Cachet, H.; Fotouhi, B.; Gorochov, O. *Semicond. Sci. Technol.* **1994**, 9, 1529

71. Zeng, A.; Bilek, M. M. M.; McKenzie, D. R.; Lay, P. A. Semiconductor properties and redox responses at a-C:N thin film electrochemical electrodes *Diamond Relat. Mater.* **2009**, 18, 1211– 1217

72. Monteiro, M. J.; Bazito, F. F. C.; Siqueira, L. J. A.; Ribeiro, M. C. C.; Torresi, R. M. Transport Coefficients, Raman Spectroscopy, and Computer Simulation of Lithium Salt Solutions in an Ionic Liquid *J. Phys. Chem. B* **2008**, 112, 2102– 2109

73. Ye, C.; Shreeve, J. M. Rapid and Accurate Estimation of Densities of Room-Temperature Ionic Liquids and Salts *J. Phys. Chem. A* **2007**, 111, 1456– 1461

74. Spear, H. E.; Dismukes, J. P. *Synthetic diamond: emerging CVD Science and Technology*; J. Wiley & Sons:New York, **1994**.

75. Wang, Z. L.; Li, J. J.; Sun, Z. H.; Li, Y. L. Effect of grain size and pores on the dielectric constant of nanocrystalline diamond films *Appl. Phys. Lett.* **2007**, 90, 133118 (3)

76. Kondo, T.; Honda, K.; Tryck, D. A.; Fujishima, A. AC impedance studies of anodically treated polycrystalline and homoepitaxial boron-doped diamond electrodes *Electrochim. Acta* **2003**, 48, 2739– 2748

77. De Gryse, R.; Gomes, W. P.; Cardon, F.; Vennik, J. On the Interpretation of Mott-Schottky Plots Determined at Semiconductor/Electrolyte Systems *J. Electrochem. Soc.* **1975**, 122, 711– 712